Journal of
Manufacturing and Materials Processing

Article

Monitoring Variability in Melt Pool Spatiotemporal Dynamics (VIMPS): Towards Proactive Humping Detection in Additive Manufacturing

Mohamed Abubakr Hassan [1,2,3], Mahmoud Hassan [2,3,*], Chi-Guhn Lee [1,2] and Ahmad Sadek [3]

[1] Centre for Maintenance Optimization and Reliability Engineering (C-MORE), Toronto, ON M5S 1A8, Canada; mahassan@mie.utoronto.ca (M.A.H.); cglee@mie.utoronto.ca (C.-G.L.)
[2] Department of Mechanical and Industrial Engineering, University of Toronto, Toronto, ON M5S 1A1, Canada
[3] Aerospace Manufacturing Technologies Center, National Research Council Canada, Montreal, QC H3T 1J4, Canada; ahmad.sadek@cnrc-nrc.gc.ca
* Correspondence: mahmoud.hassan@cnrc-nrc.gc.ca

Abstract: Humping is a common defect in direct energy deposition processes that reduces the geometric integrity of printed products. The available literature on humping detection is deemed reactive, as they focus on detecting late-stage melt pool spatial abnormalities. Therefore, this work introduces a novel, proactive indicator designed to detect early-stage spatiotemporal abnormalities. Specifically, the proposed indicator monitors the variability of instantaneous melt pool solidification-front speed (VIMPS). The solidification front dynamics quantify the intensity of cyclic melt pool elongation induced by early-stage humping. VIMPS tracks the solidification front dynamics based on the variance in the melt pool infrared radiations. Qualitative and quantitive analysis of the collected infrared data confirms VIMPS's utility in reflecting the intricate humping-induced dynamics and defects. Experimental results proved VIMPS' proactivity. By capturing early spatiotemporal abnormalities, VIMPS predicted humping by up to 10 s before any significant geometric defects. In contrast, current spatial abnormality-based methods failed to detect humping until 20 s after significant geometric defects had occurred. VIMPS' proactive detection capabilities enable effective direct energy deposition control, boosting the process's productivity and quality.

Keywords: additive manufacturing; condition monitoring; direct energy deposition; proactive; solidification front; spatiotemporal

Citation: Hassan, M.A.; Hassan, M.; Lee, C.-G.; Sadek, A. Monitoring Variability in Melt Pool Spatiotemporal Dynamics (VIMPS): Towards Proactive Humping Detection in Additive Manufacturing. *J. Manuf. Mater. Process.* **2024**, *8*, 114. https://doi.org/10.3390/jmmp8030114

Academic Editors: Zhichao Liu, Yingbin Hu and Dazhong Wu

Received: 24 April 2024
Revised: 16 May 2024
Accepted: 21 May 2024
Published: 29 May 2024

1. Introduction

Direct energy deposition (DED) stands out among additive manufacturing (AM) technologies due to its high productivity of geometries with near-to-optimal shapes. The capability of multi-axis material delivery as a powder or wire enables the creation and repair of complex geometries, large-scale parts, and multi-grade materials, aligning with the demands of aerospace applications [1–3]. This advantage of material delivery in DED comes with significant challenges. Unlike powder bed processes, where the powder is laid statically, the DED material's dynamic delivery complicates the heat dissipation [4,5]. The continuous and localized addition of material generates varying heat intensities and gradients, leading to a complex thermal profile within the heat-affected zones. This complexity in heat management can result in various defects and the absence of consistent and standardized process output characteristics. The non-uniform cooling, heat accumulation, and re-melting of built layers during the disposition of new ones leads to micro and macro defects such as geometric and dimensional distortion, surface and internal cracks, and porosity formation [6]. Consequently, a large body of literature focuses on developing different monitoring and control systems to improve the reliability and repeatability of DED processes [7].

Humping is a phenomenon that significantly reduces the geometrical accuracy of the produced products. Figure 1a shows a severe humping manifestation, demonstrating the formation of crests and valleys that contribute to the characteristic wavy structure. During humping, the melt pool goes through a series of abnormal solidification dynamics (i.e., modes). Transitioning between these different modes depends on the humping severity, as shown in Figure 1. Panels (b–f) showcase the different melt pool modes associated with humping, with the severity increasing progressively from b to f. Additionally, within each panel, time progresses from the top to the bottom (e.g., (b.1) precedes (b.2)). Starting with the normal mode, in Figure 1(b.1,b.2), the melt pool (MP) shows a temporally invariant shape. This temporal invariant shape implies that the solidification front (SF) speed matches the laser speed. Thus, the relative velocity between the laser and solidification front at the melt pool tail is almost zero. The initial stage of humping starts with the MP elongation mode. In this mode, the MP shows cyclic behavior, alternating between long (Figure 1(c.1)) and short melt pools (Figure 1(c.2)). This variation in melt pool size indicates an inconsistent solidification front velocity direction (SFD), which is the direction of the relative velocity between the solidification front and the scanning speed, as shown by the orange arrows in Figure 1(c.1,c.2). A negative SFD means that the solidification front is moving away from the laser, and the liquid is accumulating at the MP tail, as shown in Figure 1(c.1). Conversely, a positive SFD indicates liquid solidifying at the tail, causing a shorter MP. Despite this fluctuation in the SFD, the degradation of geometric accuracy is minimal during the early humping stage (i.e., elongation mode).

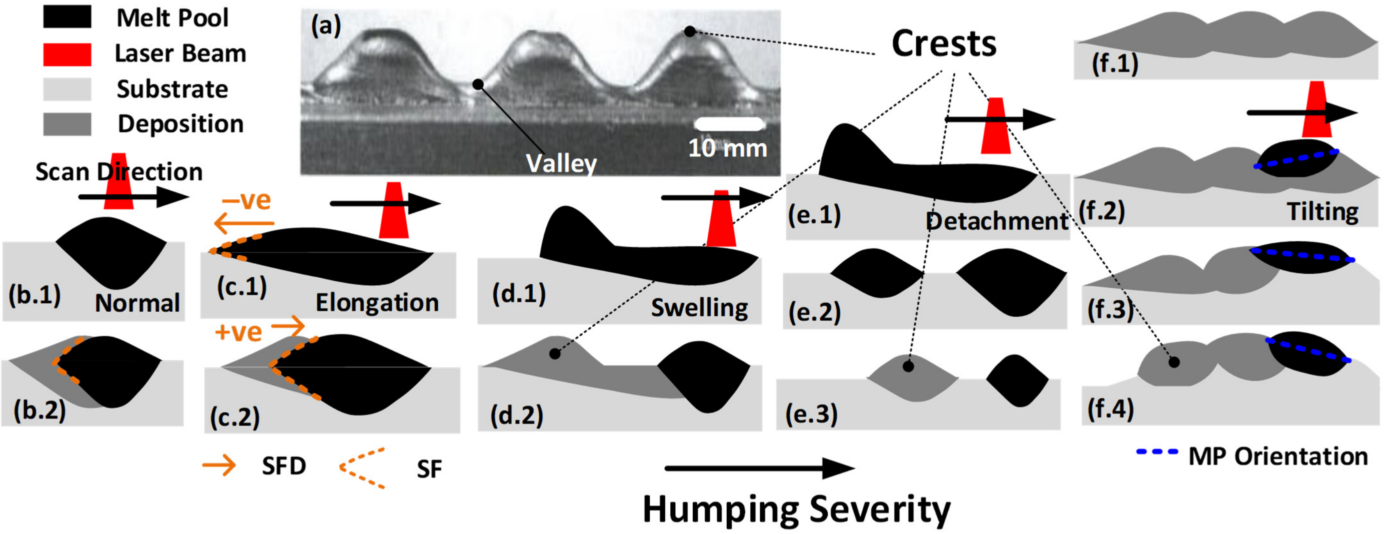

Figure 1. (**a**) Real image of severe humping redrawn from [8] showing the crests and valleys forming the wavy structure. Each column (i.e., from (**b**–**f**)) shows different melt pool modes with humping severity increasing from (**b**) to (**f**). Within each column, time progresses from top to bottom.

As the severity of humping intensifies, the process transitions from the elongation mode to the swelling mode. A significant volume of liquid accumulates at the MP's tail (Figure 1(d.1)) and solidifies locally, leading to crest formation at the tail (Figure 1(d.2)). When the elongation is excessive, the detachment mode is activated. The MP tail is detached and forms an isolated liquid volume (Figure 1(e.2)), further contributing to crest formation (Figure 1(e.3)).

During swelling mode, the continuous formation of these crests deteriorates the printed part's geometrical accuracy rendering it wavy (Figure 1(f.1)). When the surface is wavy, late humping symptoms (i.e., tilting mode) are observable. The MP follows a distorted path (i.e., wavy trajectory); thus, it starts to tilt—see the change in the MP orientation indicated by the blue line in Figure 1(f.2–f.4).

The current literature offers various contradictory mechanisms that trigger the elongation and swelling mode. Some hypothesize a relation between powder density gradients in the gas-powder jet and humping creation. They assume that the powder gradient can cause protrusion growth [9]. Such protrusions are similar to the swelling in Figure 1(d.1) and thus can also lead to the formation of the humping wavy surface in Figure 1a. However, humping is not exclusive to powder-based AM processes but is also common in non-power-based processes such as welding [10–12]. In the welding literature, humping is often related to factors such as strong forward flow momentum and limited backfilling. The process conditions that trigger these factors are still unclear. In keyhole printing, with high energy intensity and deep depression in the laser-material interaction zones, some hypothesize that the lateral oscillation of the keyhole triggers humping [13,14]. However, humping is not exclusive to the high-energy-intensity keyhole printing mode but is also observed for conduction-mode welding with lower energy intensity and shallow melt pools. Gullipalli et al., 2023 have even recently shown that reducing heat input in DED (i.e., moving from keyhole to conduction mode printing conditions) can aid in activating humping [15]. These contradictory recommendations and explanations arise from the complex non-linear interactions of physics in metal welding and printing. Thus, generalizations of these explanations or guidelines will always be doubtful, reducing the reliability of offline energy input optimization and emphasizing the need for real-time printing monitoring systems.

Instead of energy input optimization, the industry adopts energy management optimization. Energy management can occur by active cooling [16,17] or interlayer dwelling, with the latter being the more common strategy. Interlayer dwells pause the printing for a predetermined dwell time (DT) after a predetermined continuous deposition time (CDT), allowing the part to cool down and reach a predetermined temperature before resuming printing [18,19]. If achieved, optimal energy management is capable of keeping the melt pool in its normal state (Figure 1(b.1,b.2), effectively preventing humping. However, predetermining DT and CDT is a considerable optimization problem. For example, it has been shown that the optimal CDT varies depending on the printed part geometry and the current build height [20]. Frequent stopping or unnecessarily prolonged dwell reduces productivity and subjects the part to unnecessary thermal cycles, potentially degrading quality [21,22]. Conversely, excessive delays in stopping (i.e., too long CDT) may lead to irreversible geometric inaccuracies, rendering the part as scrap unless hybrid additive-subtractive manufacturing techniques are available. Therefore, identifying the optimal stopping time that maximizes the CDT is crucial, highlighting the need for advanced real-time monitoring technologies.

While there are numerous studies dedicated to online monitoring solutions for detecting humping onset in additive manufacturing, the majority are reactive rather than proactive. This is because they have focused on humping late spatial symptoms rather than early spatiotemporal dynamics [23–25]. For instance, [24] detects humping when the melt pool is spatially detached into two separate liquid volumes (i.e., the detachment mode illustrated in Figure 1(e.2)). At this stage, geometric inaccuracies caused by humping have already manifested and may lead to part scraping. Therefore, proactive monitoring of humping is crucial to provide enough time to take action to prevent irreversible geometric defects.

The principal contribution of this study is the early detection of the elongation mode of humping. Our hypothesis is that focusing on spatiotemporal abnormalities, rather than solely spatial ones, enables earlier and more accurate humping detection. This is because early detection of the elongation mode requires the simultaneous consideration of both spatial and temporal (i.e., spatiotemporal) dynamics (i.e., the variation between Figure 1(c.1,c.2)), unlike the late detachment mode, which can only be detected by identifying spatial abnormalities (i.e., the swelling state illustrated in Figure 1(e.2)). Motivated by this physical understanding, we propose the VIMPS indicator as the following:

1. Transforms from reactive to proactive humping detection.
2. Transforms humping detection from spatial (i.e., detachment) to spatiotemporal (i.e., elongation) abnormalities.
3. Practically tracks the variability in solidification front dynamics.

The structure of this study is organized as follows: Section 2 describes the experimental setup and test matrix utilized for collecting the infrared videos. Section 3 focuses on interpreting and processing the data to calculate the proposed humping indicator (VIMPS). Section 4 empirically confirms the superiority of VIMPS compared to current state-of-the-art approaches.

2. Experimental Setup

Experiments were conducted on a 3kW TRUMPF TruDiode laser (TRUMPF, Ditzingen, Germany) integrated with a six-axis CNC gantry. This system incorporated Reis Lasertec optics (Reis Lasertec, Würselen, Germany), an ILT powder nozzle (Fraunhofer Institute of Laser Technology ILT, Aachen, Germany), and a Sulzer-Metco TWIN-10 feeder (Sulzer Management Ltd, Winterthur, Switzerland). A 125 mm collimation lens, a 150 mm focal lens, a 600 µm fiber, a laser whose wavelength is 950 nm, and a spot size of D = 2.6 mm were used. Figure 2 shows the laser profile used. In this study, austenitic nickel–chromium stainless steel powder was used; it has a nominal particle size distribution between −45 and +11 µm and a chemical composition of Fe 17Cr 12Ni 2.5Mo 2.3Si 0.03C. Circular builds of 25 mm in both height and diameter were constructed under varied printing conditions, as detailed in Table 1. Three parts were printed using combinations of two laser powers, P, and two traverse speeds, v. All prints were made with an 8 g/min powder flow rate. In total, nine parts were printed, including two replicas. We focus on thin-walled (i.e., single-bead multi-layer) prints as they are the most prone to humping defects. A continuous spiral printing path was generated by rotating the table and moving the head in the positive Z direction, as shown in Figure 3.

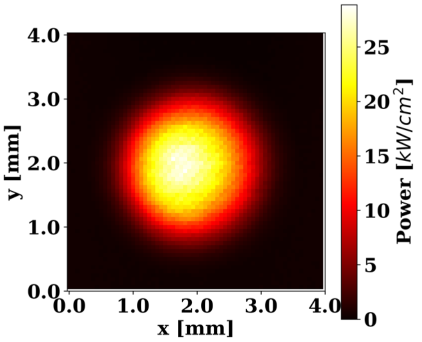

Figure 2. Laser profile used.

Table 1. Experimental test matrix.

Test No.	P (W)	v (mm/min)
1	650	600
2	650	360
3	850	360

For melt pool monitoring, a med-wave infrared MWIR camera (i.e., FLIR SC8300 (FLIR Systems, Inc., Wilsonville, OR, USA)) was used. The MWIR option was selected to ensure the capture of low-temperature regions, such as the melt pool tail, which cannot be captured by a normal *VIS* camera (i.e., a camera only sensitive to visible light). This is because visible light is mainly emitted by objects at extremely high temperatures [26]. The camera was equipped with a 50 mm focal lens with a 1-inch extension tube to achieve the desired field of view (FOV) of 5 mm × 3.5 mm. The camera was operated at a frame rate of 233 Hz and a resolution of 256 × 180 pixels. These settings were selected so that the sampling frequency was adequate to capture the humping dynamics. To allow for continuous monitoring and to negate any relative movement between the melt pool and the camera, the camera was directly mounted on the laser head, as shown in Figure 3b. After printing, the as-printed parts were imaged using a ZEISS Smartzoom 5 (ZEISS, Oberkochen, Germany) automated digital microscope to qualitatively assess the geometrical accuracy (i.e., topography).

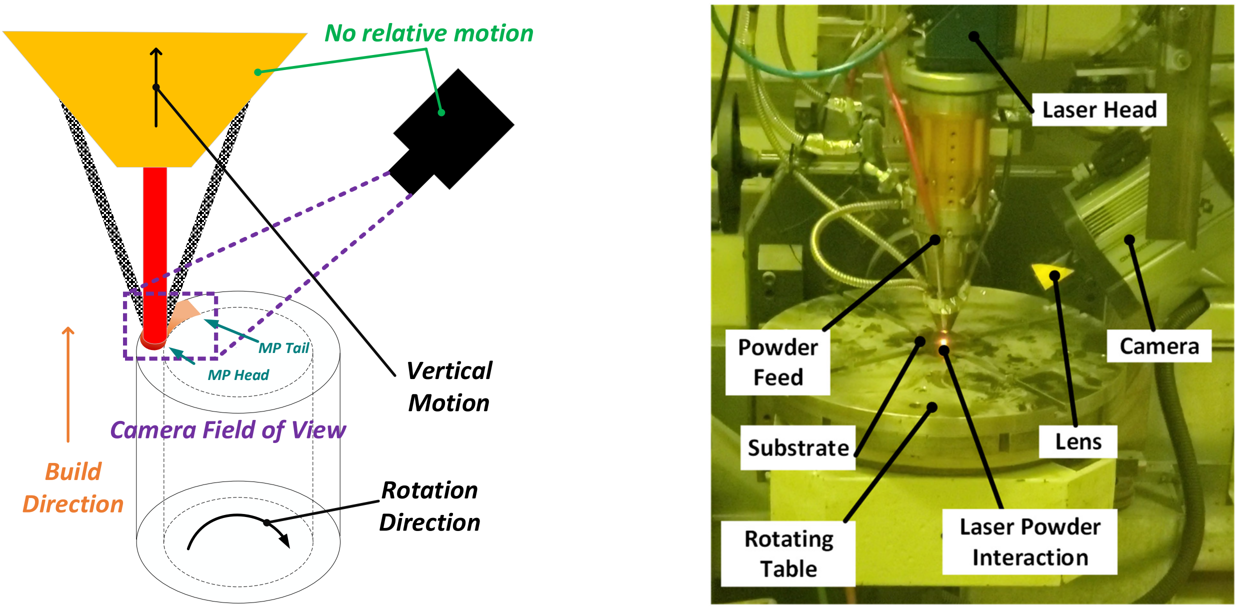

(**a**) (**b**)

Figure 3. (**a**) Schematic and (**b**) actual view of the experimental setup.

3. Signal Processing

3.1. Pixel Intensity Physical Interpretation

The present study collects the melt pool infrared signature as a series of 2D images throughout the printing duration. These sequential images provide a comprehensive overview of the melt pool spatiotemporal variations. Figure 4 shows a single frame; the top part shows the large field of view (the top image shows a zoomed-out FOV, not the processed FOV in the developed approach) of the entire cylinder, while the bottom part zooms in on the heat-affected zone (HAZ) and the melt pool. It should be noted that despite its higher temperature, the melt pool in Figure 4, marked in red, exhibits a darker appearance, indicative of lower pixel intensity. This phenomenon can be explained by the variations in emissivity associated with different phases of the material, which affect its heat radiation. According to the Stefan–Boltzmann law, the total radiation (P_{rad}) emitted by a body is a function of both its temperature (Temp) and its emissivity (ϵ), expressed as $P_{rad} = \sigma \epsilon A Temp^4$, where σ represents the Stefan–Boltzmann constant. In the case of stainless steel, the liquid phase exhibits a lower emissivity compared to its solid counterpart [27], especially when the solid is oxidized [28]. Consequently, the darker appearance of the melt pool in Figure 4 suggests that the decreased emissivity in the liquid state has a more pronounced effect than the increased temperature. Such an observation can be confirmed by analyzing the sequence of the melt pool's image after the deactivation of the laser, as shown in Figure 5. During such a sequence of images, the melt pool is solidifying; thus, its temperature consistently declines. Notably, in Figure 5, the pixel intensity of the melt pool initially increases, reaching its peak around time t = 304 s, followed by a reduction at t = 307 s. This temporary increase in pixel intensity during the solidification can be attributed solely to changes in emissivity as the material transitions from liquid to solid phases. Consequently, this explains that the lower pixel intensity of the melt pool is due to its lower emissivity. This pattern aligns with observations reported in [29], where steel displayed similar radiative characteristics during solidification in an argon environment.

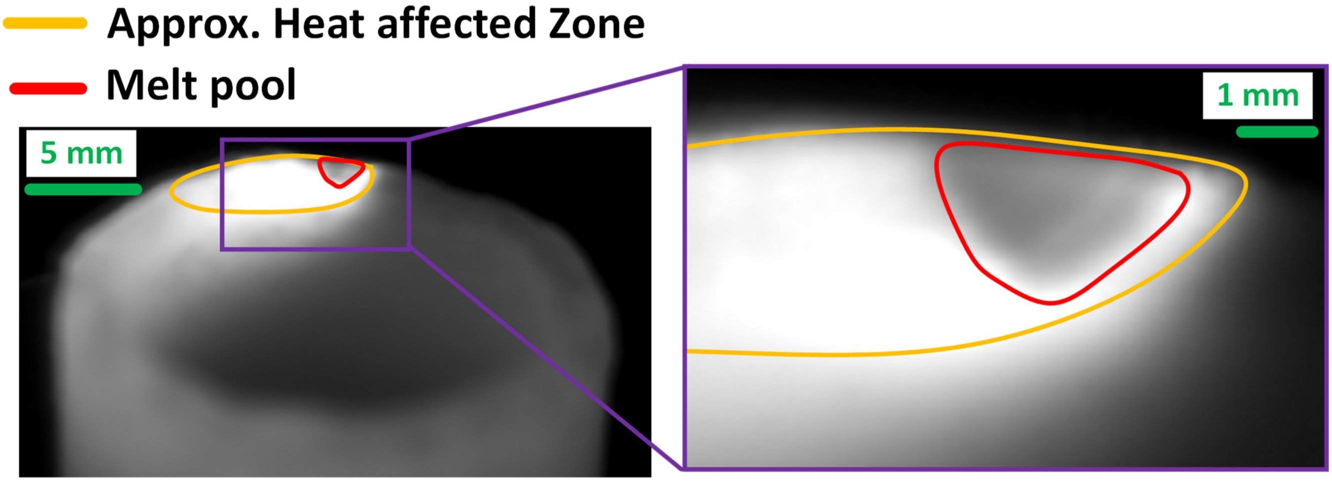

Figure 4. The melt pool and the approximate contour of the heat-affected zone (HAZ).

Figure 5. The progression of melt pool solidification after the laser was turned off. Note: t = 303.75 s corresponds to the moment at which the laser was turned off.

3.2. Physics-Based Indicator

This section outlines the proposed methodology for calculating the variability of the instantaneous MP solidification-front speed (VIMPS) indicator from the raw collected IR videos. VIMPS is designed to quantify the variability in SFD during elongation and swelling modes. The proposed method starts by defining a region of interest (ROI) around the melt pool, as shown in Figure 6. Within this ROI, for every time step, three principal indicators are computed: (1) average pixel intensity (API), (2) rolling variance of API (APIRV), and (3) rolling mean of API (APIRM). These indicators are instrumental in calculating the

VIMPS indicator. The following sections detail the computation and rationale behind these three critical indicators.

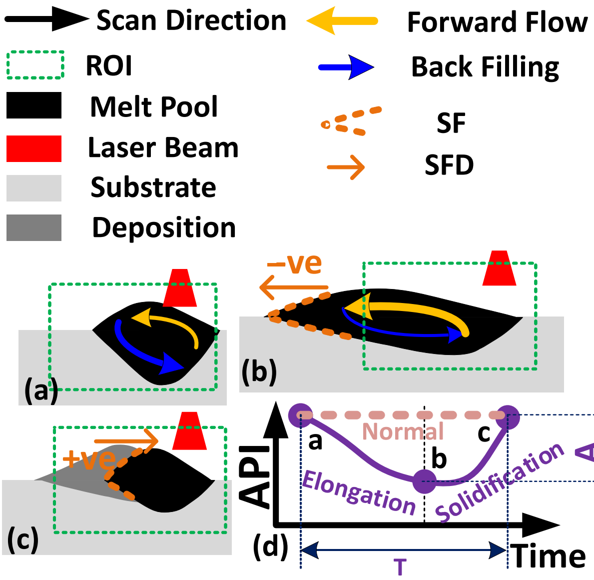

Figure 6. (**d**) Average pixel intensity (API) variations during the accumulation (**a**→**b**) and solidification (**b**→**c**) through one elongation mode cycle.

The API reflects the dominance of the solid phase over the liquid phase in the composition within the ROI. It is designed to have an inverse and positive correlation with the MP size and the SFD, respectively, as shown in Table 2. It can be calculated at a specific time step as follows (When the context is clear, the time index (t) is dropped from API(t) and $PI\ (x, y, t)$ to avoid cluttered notation. But it should be clear that each of API, APIRV, APRIVM, APRIVxM, and PI varies over time):

$$\text{API} = \frac{1}{W \times H} \sum_{x=1}^{W} \sum_{y=1}^{H} PI\ (x, y) \quad (1)$$

where W and H are the width and height of the ROI, respectively. $PI(x, y)$ represents the pixel intensity at coordinates (x, y) in the IR-captured video frame. According to Section 3.1, PI is higher for the solidified stainless-steel powder used in this study. Consequently, API is higher when the solid phase dominates the ROI composition. For example, Figure 6 shows the API variations during the accumulation and solidification through one elongation mode cycle. In Figure 6a, when the melt pool is small, the ROI composition is dominated by the solid phase; thus, API is high, as shown in Figure 6d. Driven by limited backfilling and dominant forward flow, as illustrated in Figure 6b, liquid **accumulates** within the melt pool tail, and the SFD switches to the negative direction, denoting the onset of the elongation mode. This elongation mode shifts the ROI composition towards the liquid phase, reducing the API, as Figure 2d illustrates. This API drop is due to the liquid's lower PI. Upon reaching maximal extension, the MP undergoes rapid cooling, reversing the SFD, and leading to a localized **solidification** in the tail, as shown in Figure 6c. This solidification dominates the ROI and increases the PI, thus increasing the API. Such an accumulation–solidification cycle, summarized in Table 2, will repeat throughout the elongation mode, fluctuating SFD between positive and negative values. Such fluctuations are reflected on the API, leading to the cycle shown in Figure 6c. The cycle amplitude (A) and period (T) depend on the humping intensity; small T and large A indicate intense humping. In contrast, during the normal mode (i.e., no humping), as shown by the horizontal straight line in Figure 6d, the API remains unchanged (i.e., T → ∞, A → 0) as SFD remains at zero. The subsequent steps to calculate the VIMPS indicator are essential signal-processing steps designed to minimize noise, enhance robustness, and streamline decision-making processes.

Table 2. Variation of different physical quantities during the elongation mode.

	MP Size	**SFD**	**API**
Accumulation in Figure 1(c.1)	Increasing	Negative	Decreasing
Solidification in Figure 1(c.2)	Decreasing	Positive	Increasing

Instead of calculating the cycle amplitude (A) and period (T) to quantify humping intensity, the rolling variance of API (APIRV) is used. APIRV calculates the variance in API as follows:

$$\text{APIRV} = \frac{1}{T_{RD}} \sum_{\tau=0}^{T_{RD}-1} (\text{API}(t-\tau) - \text{APIRM})^2 \tag{2}$$

where T_{RD} is the rolling window duration, τ is a time step within the rolling window, t is the current time step. In this study, T_{RD} was set to 2 s, and APIRM is the API rolling mean defined in Equation (3). Compared to the (A, T), APIRV is more straightforward to calculate as it does not involve frequency analysis and still provides the information needed for humping detection. Small (T) and large (A) are reflected as high APIRV. Thus, a sudden increase in APIRV indicates the MP transitioning from normal to elongation mode.

The rolling mean of API (APIRM) is also used to enhance the robustness of APIRV by making it less sensitive to variances that are unrelated to elongation and is calculated as follows:

$$\text{APIRM} = \frac{1}{T_{RD}} \sum_{\tau=0}^{T_{RD}-1} \text{API}(t-\tau) \tag{3}$$

APRIVxM, the more robust version of APRIV, is calculated as follows:

$$\text{APIRVxM} = \text{APIRM} \times \text{APIRV} \tag{4}$$

In the calculated APRIVxM, since APIRM is low at early layers (i.e., low total heat input), it dampens the APIRV. This dampening improves robustness against unrelated variances, particularly noticeable during the initial layers, where APIRV's increase is not attributable to elongation but to initial MP formation and heat dissipation into the substrate.

Finally, the VIMPS is obtained by taking the rolling mean of the APIRVxM. The rolling mean makes VIMPS more interpretable by further dampening APIRVxM noise.

$$\text{VIMPS} = \frac{1}{T_{RD2}} \sum_{\tau=0}^{T_{RD2}-1} \text{APIRVxM}(t-\tau) \tag{5}$$

T_{RD} was set to 10 s to minimize the noise while preserving the signal information. Since API tracks the fluctuation in the instantaneous solidification front speed, and since VIMPS tracks the variability in API, the proposed indicator is the denoted variability of instantaneous melt-pool solidification front speed (VIMPS). The procedures to obtain VIMPS are summarized in Table 3.

Table 3. Pseudocode for physics-based indicator methodology.

```
Define Region of Interest (ROI)
For each time step $t$ do:
    Calculate Average Pixel Intensity (API) as per Equation (1)
    Calculate API's Rolling Mean (APIRM) as per Equation (2)
    Calculate API's Rolling Variance (APIRV) as per Equation (3)
    Calculate APIRVxM as per Equation (4)
    Calculate (VIMPS) as per Equation (5)
End For
```

4. Results

The results of this study are divided into three sections: Section 4.1 provides an overview of the outcome of the tests in the test matrix shown in Table 1. Section 4.2 affirms the VIMPS expressiveness of the geometrical defect, while Section 4.3 affirms API's capability to track the solidification dynamics, which is essential for VIMPS's success.

4.1. Geometrical Accuracy

Figure 7 shows the as-printed parts of the different tests in Table 1. Figure 7a–c shows isometric views of the parts, while Figure 7d–f presents top-view images of the printed parts alongside the surface topography (i.e., the inner circle color map). Parts printed in Tests #1 and #3 have shown signs of humping. Figure 7a,d clearly shows the geometrical defects caused by melt-pool humping. More specifically, in Figure 7d, the unstable deposition and swelling formed a crest valley structure, as shown in the top view surface topography. In addition, the effect of humping can also be seen by looking at the side walls of the cylinder in Figure 7a,c. It is observed that there are protrusions, normal to the cylinder wall, indicative of the swelling and uneven deposition that is associated with humping. More interestingly, the protrusions in Figure 7c form a spiral pattern, which will be explained later in Section 4.2. Most importantly, Test #2 shows an acceptable geometrical shape with no signs of humping, as shown in Figure 7b,e.

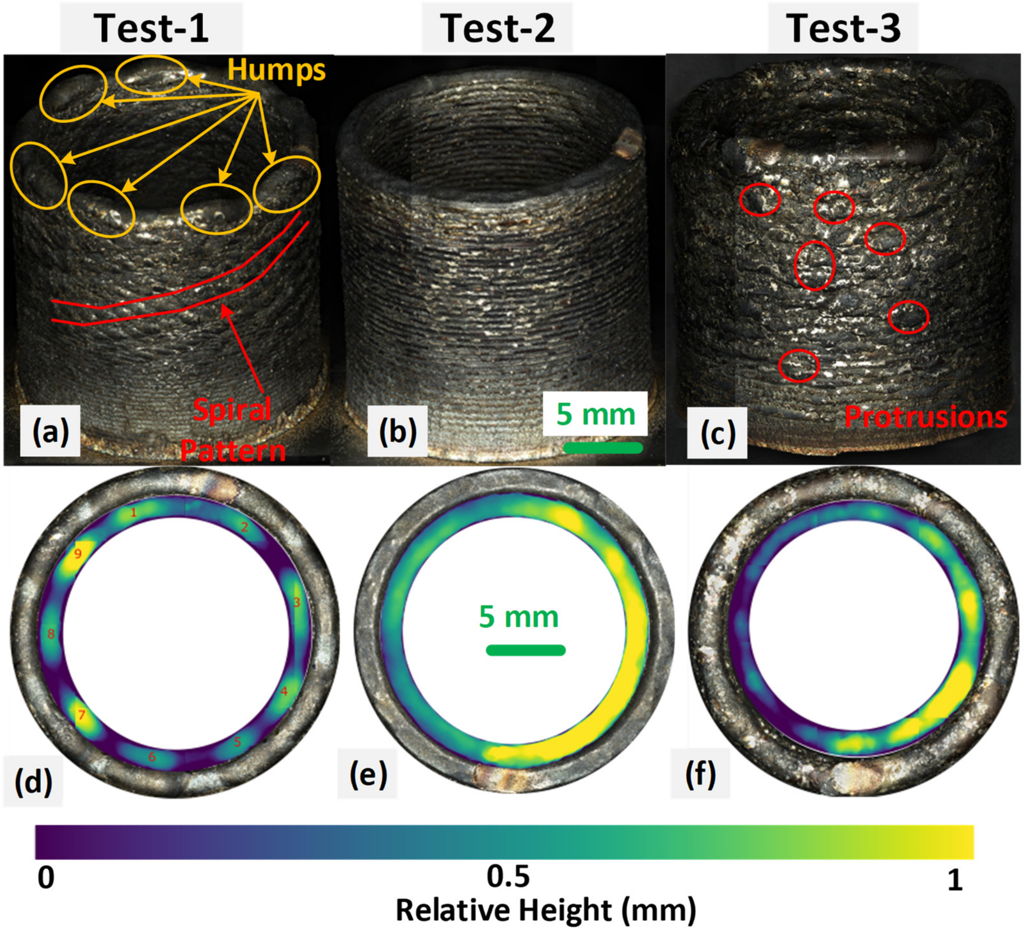

Figure 7. As-printed parts. (**a**,**d**) Test-1, (**b**,**e**) Test-2, and (**c**,**f**) Test-3. (**d**–**f**) Top-view with an elevation map (i.e., topography). Yellow regions are higher than blue regions by 1 mm, as shown in the scale. Note that the variations in (**e**,**f**) are mainly due to the helical printing path, while in (**d**), the variations are dominated by the humping-induced crests.

In terms of humping in relation to printing conditions, Gullipalli et al. [17] suggested that lower heats activate humping. However, our experiments show a contradicting trend where lower heats suppressed humping. Comparing Test #2 to Test #1 in Figure 6 shows less protrusion in Test #2 (i.e., Figure 6b) compared to Test #1 in Figure 6a. This is despite the low heat input for Test #2 (i.e., higher speed), as shown in Table 1. The contradiction between the trend seen here and the one seen in Gullipalli et al. [17] indicates that it is challenging to draw a simple relation between the process parameters and humping activation. The complexity arises from the non-linear interplay of various physical factors involved. Therefore, the development of real-time condition-monitoring systems, such as VIMPS, is vital for real-time control and elimination of humping.

4.2. VIMPS Expressiveness of Geometrical Defects

As will be demonstrated in this Section, VIMPS shows a clear correlation to the geometric defects presented in Figure 7. Figure 8 shows API, APIRV, and VIMPS for the three prints shown in Figure 7. The bottom x-axis indicates the time elapsed since the beginning of the print process, while the top x-axis indicates the layer number. The API is indicated on the left y-axis, whereas the APIRV and VIMPS values are plotted on the right y-axis. A vertical line marks the layer and time—referred to as T*Geo—when geometric protrusions start to appear on the as-printed part. Notably, the upsurge in VIMPS values consistently aligns with T*Geo across all samples, affirming the indicator's predictive value for detecting early humping modes (i.e., elongation). Additionally, Figure 8 shows the usefulness of the signal processing steps performed to calculate VIMPS based on the APIRV. VIMPS is significantly more interpretable and has lower noise than APIRV.

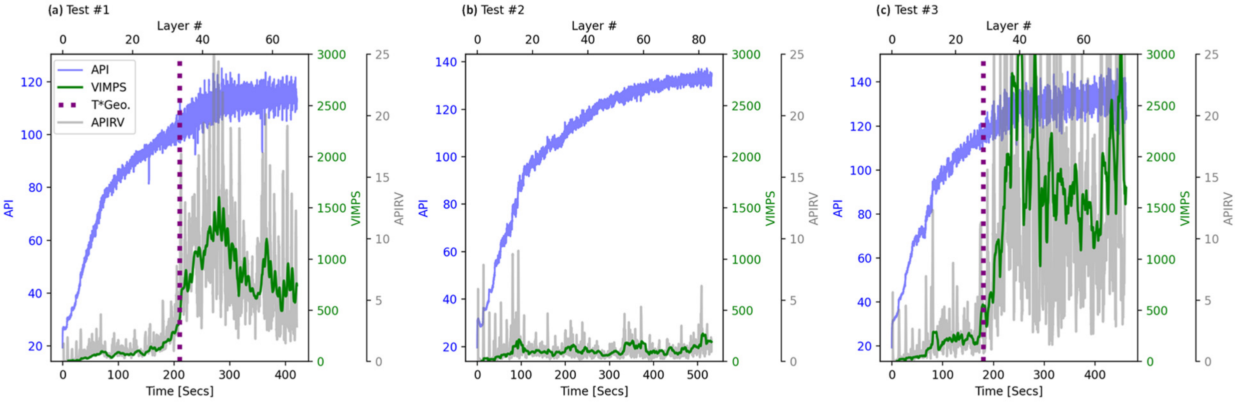

Figure 8. Variability of instantaneous melt pool solidification-front speed (VIMPS) for different prints. (**a**) Test #1 (**b**) Test #2 (**c**) Test #3.

To demonstrate the correlation between VIMPS and the humping-induced geometric inaccuracy, Figure 9 shows the VIMPS overlayed on a sectioned surface topography of Test #3. The surface topography further highlights the existence and location of protrusions induced by humping, as shown earlier in Figure 7c. In Figure 9a, these protrusions appear as yellow bright spots. Such spots result from the sudden and localized solidification highlighted earlier in Figure 1 during swelling modes. More importantly, when VIMPS is overlayed on the topography in Figure 9a, the noticeable increase in VIMPS matches the building height at which the protrusion starts to appear more frequently (i.e., protrusion density). Note that in Figure 9a, the x-axis (i.e., location) is shared but not the y-axis. This alignment between VIMPS and the density of the protrusions further confirms the utility of VIMPS for both humping detection and quantification.

Table 4 summarizes the superiority of VIMPS over the spatial-based SOTA in terms of latency, computations, and consistency, whereas Figure 10 shows the onset of the detachment mode, a severe humping condition, in Tests 1 and 3. Available SOTA approaches in the literature detect humping by monitoring the detachment mode, and hence, their detection of humping is expected to be at or after the onset of detachment mode, as shown in Figure 10. In Test #1, VIMPS detected humping at approximately t = 200 s, well ahead of the first realization of detachment mode at t = 219.07 s, as demonstrated in Figure 10a. Thus, VIMPS lowered the detachment latency by almost 20 s. The superiority of VIMPS is also maintained in Test #3. As shown in Figure 10c, the detachment started at t = 200.55 s, while VIMPS had already signaled the humping at around t = 170 s, with the geometric defects observable shortly thereafter (i.e., T*Geo). VIMPS's lower latency is essential for timely interventions that can significantly enhance the manufacturing process's productivity and allow for proactive actions.

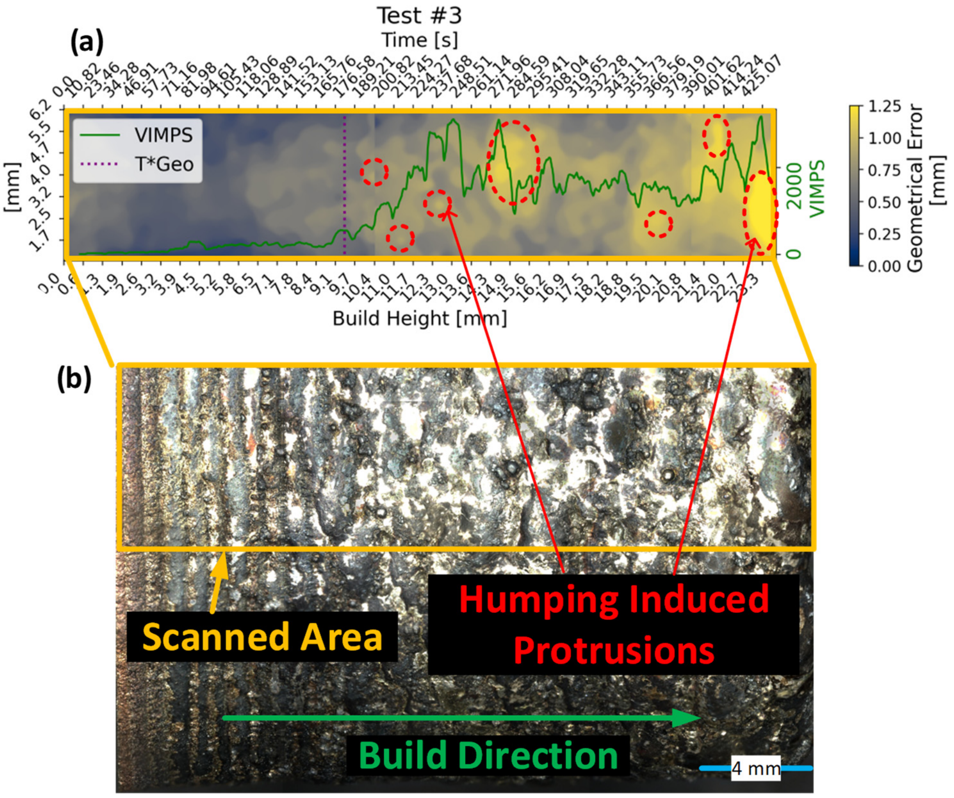

Figure 9. (**a**) Variability of instantaneous melt pool solidification-front speed (VIMPS) overlayed over the as-printed part's surface topography. (**b**) Side view of the as-printed part, highlighting the scanned surface topography shown in subfigure (**a**) in the same Figure.

Table 4. Comparative analysis of humping detection methods; all values are in seconds.

Metric	**VIMPS**		**SOTA's [24] Theoretical Upper Bound**	
Test #	1	3	1	3
Detection Time	200	170	219	200
T*Geo Time	210	180	210	180
Detection Lead	10	10	−9	−20
Consistency	High		Low	
Complexity	Low		High	
Principle	Spatiotemporal		Spatial	
Mode	Elongation		Detachment	

Note that this is an upper bound for the SOTA performance, as detachments in this figure were detected by human annotator. In reality, lower performance is expected due to error depending on the segmentation approach used.

Regarding consistency, Figure 10b,d shows the second occurrence of MP detachment in the respective tests. It is noticeable that this second occurrence is delayed up to 44.45 s, as shown in the case of Test #1. This low consistency (i.e., the lag between the first and second occurrence) lowers the operator's confidence in the detachment-based SOTA and complicates the decision making. On the other hand, Figure 8 shows that VIMPS is consistently and significantly higher after the T*Geo. In addition, the simplicity of VIMPS offers a practical advantage over the detachment-based SOTA. This is because the detachment-based SOTA requires a more sophisticated segmentation algorithm to detect when the MP is detached into separate volumes. Although many segmentation approaches have been proposed lately, they are still more complex than VIMPS and, thus, more prone to error. For example, Appendix A shows the result of segmenting Figure 10a using the "Segment Anything Model" (SAM) [30], a SOTA segmentation model. Despite its sophistication, SAM fails to segment the melt pool correctly without human help; a detailed explanation of this conclusion is available in Appendix A. Accordingly, VIMPS effectively addresses several critical issues inherent in the detachment-based SOTA:

1. It corrects the conceptual oversight related to the early stages of humping elongation modes.
2. It acknowledges the temporal dynamics of humping, which are often overlooked.
3. It avoids the complexity of segmentation, reducing potential errors.

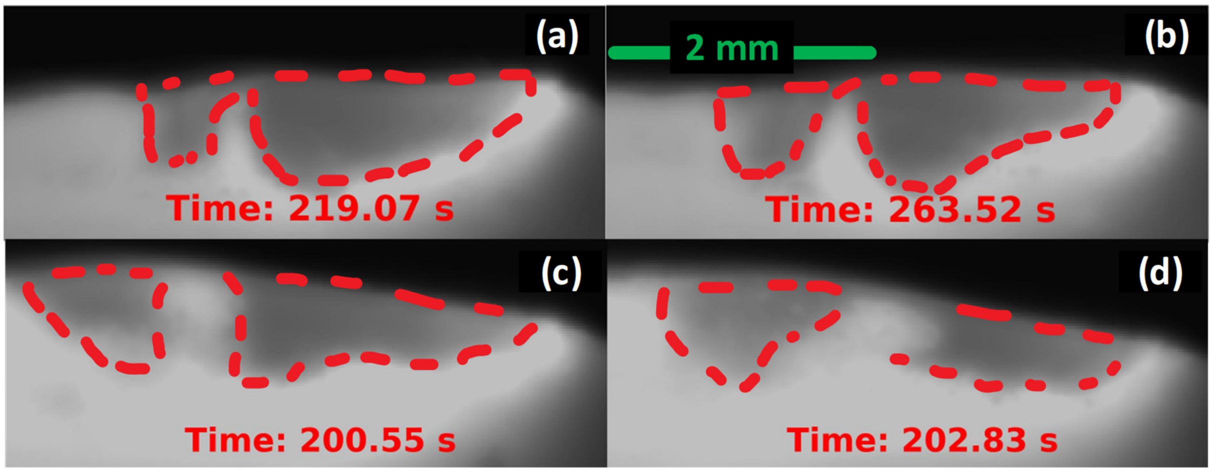

Figure 10. Manually annotated melt pool at the detachment mode (**a**,**b**) from Test #1 and (**c**,**d**) from Test #3. (**a**,**c**) First instances of the detachment mode in the corresponding test and (**b**,**d**) the second instance.

These improvements over the detachment-based approach are summarized in Table 4, highlighting the benefits and enhanced reliability of using VIMPS.

The following analysis focuses on calculating the tilting frequency, another helpful insight that is lost if temporal variations are overlooked. Figure 11 shows the result of performing fast Fourier transformation (FFT) on the API signal during MP tilting. As shown in Figure 11a, the API signal shows a quasi-sinusoidal pattern with a dominant frequency of 1.22, as shown in Figure 11b. This frequency is 9.4 times the table rotation frequency (i.e., 0.13 Hz) during the cylinder printing process, which can be directly related to the nine distinct crests observed in Figure 7d and the spiral pattern observed in Figure 7a. The melt pool completes approximately nine tilt cycles in each layer according to the dominant frequency, reflecting the nine crests shown at the top layer of the print. The spiral pattern arises because the humping frequency is not an exact multiple of the rotation frequency. Therefore, with each successive layer, the crests' location shifts by an angle of $\delta\theta$. This can be conceptualized as stacking various elevation maps from Figure 7d, with each layer rotating by $\delta\theta$, leading to the spiral formation observed in Figure 7a. The alignment between the insights from Figure 11 and the as-printed part geometry shown in Figure 7 affirms the efficacy of API to reflect the MP's spatiotemporal dynamics and its real-time expressiveness of geometrical defect occurrence and characteristics. Additionally, this highlights the usefulness of monitoring the temporal information that, unlike VIMPS, current SOTA approaches overlook.

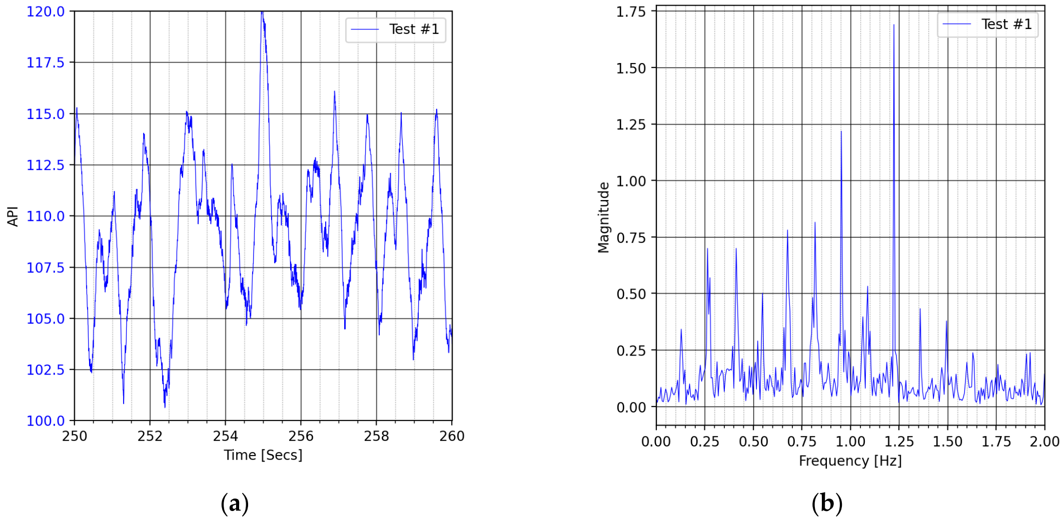

Figure 11. (**a**) Average pixel intensity (API) during tilting in Test #1 (i.e., layer-32 to layer-44) and (**b**) its fast Fourier transformation analysis.

Although Figure 7b reveals no visible meso-protrusions in Test #2, Figure 12 shows some micro-protrusions when the topography is investigated with higher resolution. These micro-protrusions especially appear towards the late layers, as shown in Figure 12c. The size of these micro-protrusions can vary significantly. For example, Figure 12b shows two adjacent micro-protrusions, each with a unique topography. It is worth noticing that these micro-protrusions are generally larger than the powder size used in this study.

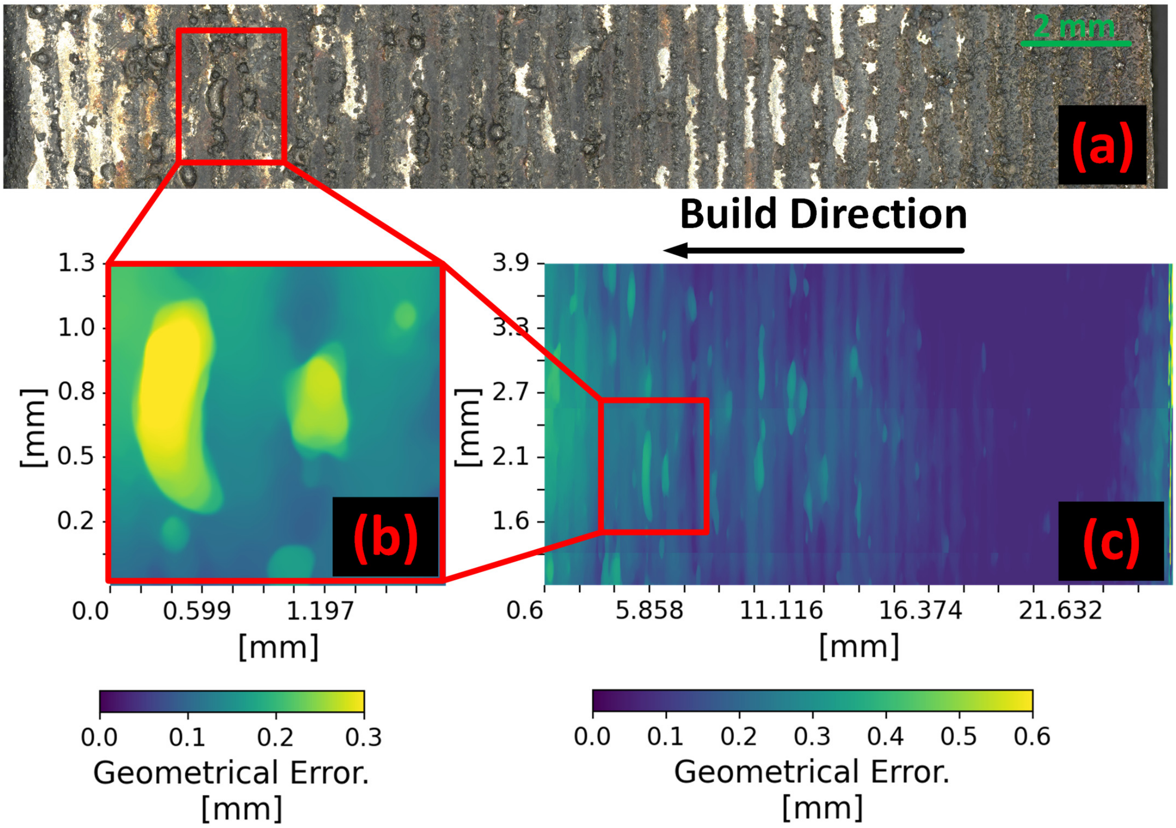

Figure 12. Micro-protrusion during Test #2. (**a**) A strip from the side wall, (**b**,**c**) topography of a small protrusion, and the entire strip, respectively.

4.3. API Expressiveness of Solidification Spatiotemporal Dynamics

The superiority of VIMPS is conditioned on the API's success in tracking the solidification's spatiotemporal dynamics. This section affirms API's expressiveness regarding the elongation cycle's spatiotemporal dynamics. Figure 13a,b shows the elongation mode's cycle (i.e., accumulation and solidification steps) during Test #1. Test 1's early layer is shown in column (a), while the late layer is shown in (b). The liquid accumulation starts in Figure 13(a.1,b.1), and the melt pool reaches its maximum elongation at the end of liquid accumulation in Figure 13(a.2,b.2). The resultant increased surface area of the melt pool then speeds up cooling, leading to localized solidification at the tail, Figure 13(a.3,b.3). These steps are more distinguishable in the melt pool infrared image at late humping stages (i.e., Figure 13b) compared to the early stage (i.e., Figure 13a). This is because the elongation is much smaller in the early stage compared to the late layers.

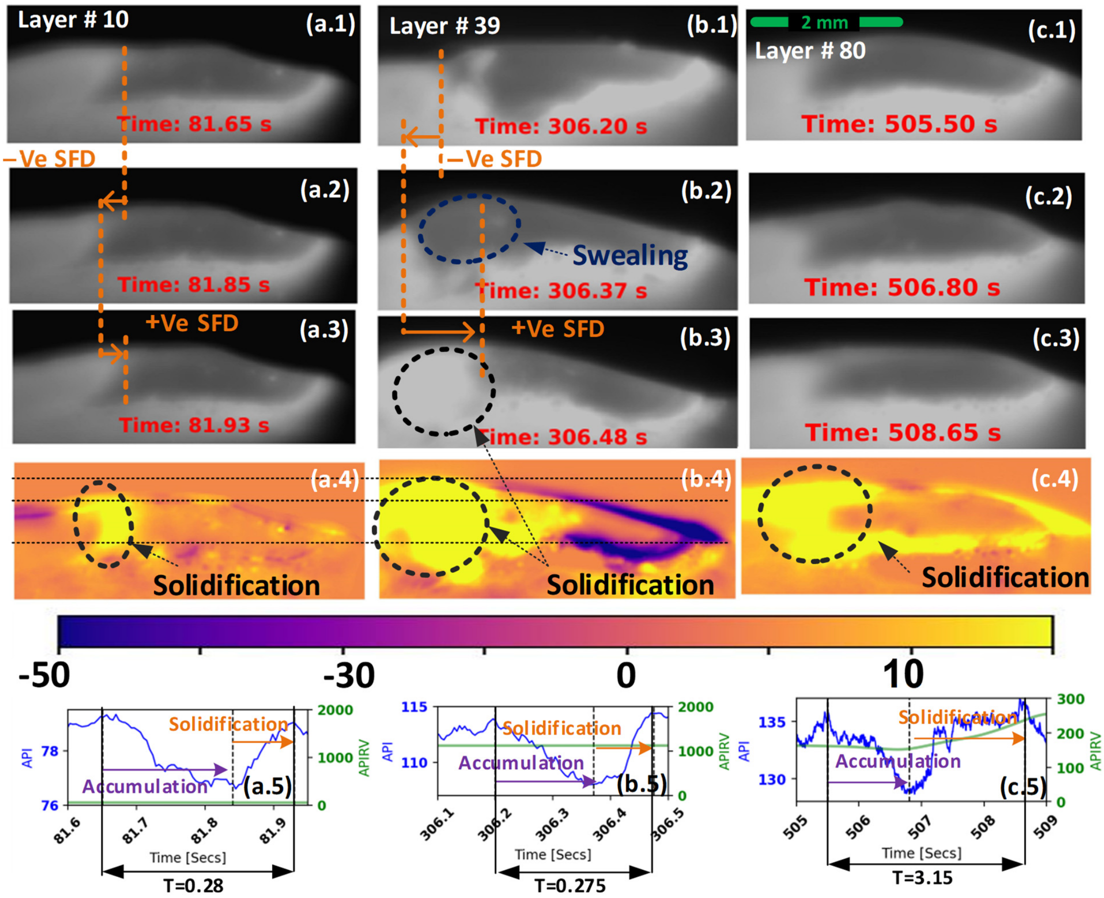

Figure 13. (**a**) Early and (**b**) late infrared images from test #1 and (**c**) late test #2. The accumulation step begins in (1) and ends in (2), and the solidification step starts in (2) and ends in (3). Subplots (4) show the pixel intensity increase during the solidification (i.e., the pixel-wise difference between (3) and (2). Subplots (5) show the average pixel intensity (API) and variability of instantaneous melt pool solidification-front speed (VIMPS) variation during the elongation cycle.

To highlight the distinctions in solidification spatiotemporal dynamics between the early and late layers, Figure 13(a.4,b.4) captures the pixel intensity (PI) increase resulting from solidification processes. The PI increase over time is critical to reveal the spatiotemporal dynamics because, unlike the spatial variations shown in Figure 10, the spatiotemporal difference is hidden if only a single frame (i.e., single time step) is investigated. Figure 13(a.4) demonstrates the pixel-wise difference between Figure 13(a.3,a.2), where the pronounced yellow regions signal the formation of new solid structures and switching the SF to the positive direction, as shown in Figure 13(a.3,a.2). At the late layer, under the swelling mode, the accumulated liquid at the tail locally solidifies, as shown in Figure 13(b.3,b.2), forming a crest that elevates well above the MP head, as shown in Figure 13(b.3).

The VIMPS design takes advantage of the API's ability to reflect the intricate elongation and swelling spatiotemporal dynamics. Figure 13(a.5,b.5) confirms the previously conceptualized trend in Figure 6d, where the API exhibits a decreasing trend with the liquid's accumulation at the melt pool's tail, followed by an increasing trend during solidification. This API trend aligns with the phase transformation during solidification, regardless of the magnitude of the elongation. The intensity of API fluctuations (i.e., amplitude and frequency) correlates directly with the MP abnormal solidification front's spatiotemporal dynamics. Consequently, quantifying the API fluctuation leads to the novel proposed VIMPS indicator. It is worth noticing that in Figure 13(b.4), the head of the melt pool shows a negative value (i.e., blue shades), which is unrelated and even contradicts the SF dynamics at the tail. Future work can test excluding the MP head from the analyzed ROI and how this will affect the quality of the API signal.

Figure 13(c.5) also shows interesting insights correlating Test #2's overall relatively good geometrical accuracy with its solidification dynamics. For Test #2 in Figure 13(c.5), the elongation cycle time (T) is significantly higher than the other two tests in Figure 13(a.5,b.5). Test #2 takes 3.15 s to complete one cycle, while it took 0.28 s for the other two tests. This indicates that the elongation mode is activated in both, especially toward the end layers, but with a longer cycle time in the case of Test #2.

5. Conclusions

Motivation: This study addresses the limitations of offline humping elimination methods and the high detection lag in current online approaches. This work hypothesizes that monitoring spatiotemporal abnormalities enables earlier humping detection. To test this hypothesis, a new proactive monitoring indicator is introduced, which monitors the variability of instantaneous melt pool solidification-front speed (VIMPS).

Methodology: VIMPS captures the unique spatiotemporal dynamics of the solidification front. Unlike traditional methods that focus on spatial abnormalities, VIMPS analyzes the average pixel intensity (API) in infrared video data to detect early elongation modes. This method identifies cyclic fluctuations in the solidification front speed, which correspond to the early stages of humping. By quantifying these fluctuations, VIMPS provides a proactive humping indicator.

Key findings: The results confirmed our hypothesis. Thanks to monitoring spatiotemporal abnormalities, VIMPS proactively detected humping 10 s before its onset. In contrast, current spatial abnormalities based on state-of-the-art methods only reactively detect it up to 20 s after its initiation. This results in a reduced detection latency of up to 30 seconds, a significant improvement over existing methods. This reduction in latency is crucial for DED process optimization and control. Additionally, the FFT analysis confirmed API's ability to reflect the intricate patterns of humping-induced defects.

Impact: For industrial applications, VIMPS is computationally efficient and utilizes existing hardware, making it easy to integrate into current monitoring systems. As a practical and proactive indicator, VIMPS serves as a crucial first step toward achieving real-time DED optimization and control.

Supplementary Materials: The following supporting information can be downloaded at: https://www.mdpi.com/article/10.3390/jmmp8030114/s1, Figure S1: MP (melt pool) infrared image during detachment mode.

Author Contributions: All authors contributed to the study's conceptualization and design. M.A.H. performed material preparation and data collection. M.A.H. and M.H. developed and conducted the methodology, validation, and formal analysis. C.-G.L. and A.S. provided supervision and resources. M.A.H. wrote the first draft of the manuscript, and all authors commented on previous versions. All authors have read and agreed to the published version of the manuscript.

Funding: This research received no external funding.

Data Availability Statement: Data available upon request.

Conflicts of Interest: The authors declare no conflicts of interest.

Abbreviations

A	The amplitude of the elongation cycle
API	Average pixel intensity
CDT	Continuous deposition time
DED	Direct energy deposition
DT	Dwell time
LE	Linear energy input
MP	Melt pool
SF	Solidification front
SFD	Solidification front relative velocity direction
T	Duration of the elongation cycle
VIMPS	Variability of instantaneous melt-pool solidification-front speed

Appendix A

This appendix is meant to show the technical difficulty with the current state-of-the-art method (SOTA). As discussed in Section 4.2, the detachment-based SOTA involves using image segmentation to determine when the melt pool (MP) divides into separate volumes. Image segmentation has garnered significant attention in additive manufacturing (AM) research, leading to various successful models tailored to specific AM-related segmentation problems [31]. On the contrary, the Segment Anything Model (SAM) [30], developed by Meta, stands out due to its zero-shot learning capabilities, which allow it to operate across new datasets without further training or finetuning.

Zero-shot learning is a valuable attribute as it eliminates the need for manually annotated datasets, which is a major time-consuming and labor-intensive step in developing deep learning models. This attribute aligns with the simplicity offered by the VIMPS tool. However, our empirical analysis, illustrated in Figure A1, demonstrates that SAM struggles with correct segmentation without human guidance (i.e., SAM "Everything" prompting). Even when the model is given extra information through supervised inference (i.e., "Hover and Click". Promting), it still struggles. In the "Hover and Click" mode, during inference, the user iteratively adds blue dots at regions that belong to the melt pool and adds red points to areas that do not. In detachment mode, it becomes more challenging as the user needs to define two isolated melt pool volumes and insert red dots into the proper regions to split the segmented region into two separate volumes properly. So, even with supervision, detachment detection is challenging. For real-time monitoring, the segmentation inference should be fully unsupervised.

This limitation underscores a critical limitation of zero-shot learning—while promising, it does not universally guarantee effective performance across all data sets [32]. The discrepancy between the images used in initial training and those in application settings can be substantial, often necessitating the use of transfer learning techniques to bridge this gap [33,34].

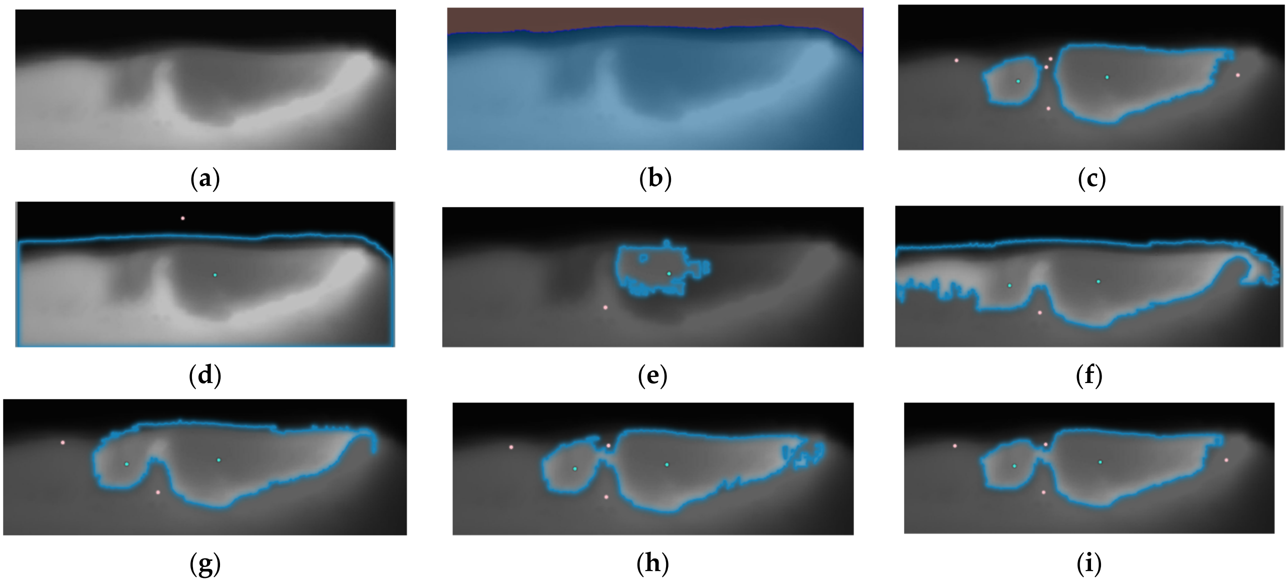

Figure A1. (**a**) MP (melt pool) infrared image during detachment mode, the same as in Figure 10a. (**b**–**i**) SAM (Segment Anything Model) segmentation results. (**b**) Zero-shot segmentation results without human aid, (**c**) the results with human aid that lead to correct segmentation, and (**d**–**f**) the intermediate steps between (**b**,**c**). Interested readers can reproduce this experiment by downloading (**a**) from the Supplementary Material and testing the SAM demo on the following link [35]. (**b**) Can be obtained using the automatic "Everything" prompting, but (**c**–**f**) needs more sophisticated prompting with interactive points using the manual "Hover and Click".

References

1. Liu, Z.; He, B.; Lyu, T.; Zou, Y. A Review on Additive Manufacturing of Titanium Alloys for Aerospace Applications: Directed Energy Deposition and Beyond Ti-6Al-4V. *JOM* **2021**, *73*, 1804–1818. [CrossRef]
2. Chen, H.; Liu, Z.; Cheng, X.; Zou, Y. Laser deposition of graded γ-TiAl/Ti2AlNb alloys: Microstructure and nanomechanical characterization of the transition zone. *J. Alloys Compd.* **2021**, *875*, 159946. [CrossRef]
3. Ye, J.; Bab-hadiashar, A.; Alam, N.; Cole, I. A review of the parameter-signature-quality correlations through in situ sensing in laser metal additive manufacturing. *Int. J. Adv. Manuf. Technol.* **2023**, *124*, 1401–1427. [CrossRef]
4. Yu, T.; Chen, L.; Liu, Z.; Xu, P. Research on the temperature control strategy of thin-wall parts fabricated by laser direct metal deposition. *Int. J. Adv. Manuf. Technol.* **2022**, *122*, 669–684. [CrossRef]
5. Mianji, Z.; Kholopov, A.; Binkov, I.; Klimochkin, K. Experimental and Numerical Study of Heat Transfer in Thin-Walled Structures Built by Direct Metal Deposition and Geometry Improvement via Laser Power Modulation. *Lasers Manuf. Mater. Process.* **2023**, *10*, 353–372. [CrossRef]
6. Svetlizky, D.; Das, M.; Zheng, B.; Vyatskikh, A.L.; Bose, S.; Bandyopadhyay, A.; Schoenung, J.M.; Lavernia, E.J.; Eliaz, N. Directed energy deposition (DED) additive manufacturing: Physical characteristics, defects, challenges and applications. *Mater. Today* **2021**, *49*, 271–295. [CrossRef]
7. Tang, Z.J.; Liu, W.W.; Wang, Y.W.; Saleheen, K.M.; Liu, Z.C.; Peng, S.T.; Zhang, Z.; Zhang, H.C. A review on in situ monitoring technology for directed energy deposition of metals. *Int. J. Adv. Manuf. Technol.* **2020**, *108*, 3437–3463. [CrossRef]
8. Adebayo, A.; Mehnen, J.; Tonnellier, X. Limiting Travel Speed in Additive Layer Manufacturing. In Proceedings of the 9th International Conference on Trends in Welding Research, Chicago, IL, USA, 4–8 June 2012.
9. Turichin, G.; Zemlyakov, E.; Klimova, O.; Babkin, K. Hydrodynamic instability in high-speed direct laser deposition for additive manufacturing. *Phys. Procedia* **2016**, *83*, 674–683. [CrossRef]
10. Nguyen, T.C.; Weckman, D.C.; Johnson, D.A.; Kerr, H.W. The humping phenomenon during high speed gas metal arc welding. *Sci. Technol. Weld. Join.* **2005**, *10*, 447–459. [CrossRef]
11. Soderstrom, E.; Mendez, P. Humping mechanisms present in high speed welding. *Sci. Technol. Weld. Join.* **2006**, *11*, 572–579. [CrossRef]
12. Zhang, M.; Liu, T.; Hu, R.; Mu, Z.; Chen, S.; Chen, G. Understanding root humping in high-power laser welding of stainless steels: A combination approach. *Int. J. Adv. Manuf. Technol.* **2020**, *106*, 5353–5364. [CrossRef]
13. Yinglei, P.; Jiguo, S. Understanding humping formation based on keyhole and molten pool behaviour during high speed laser welding of thin sheets. *Eng. Res. Express* **2020**, *2*, 025031. [CrossRef]
14. Ai, Y.; Jiang, P.; Wang, C.; Mi, G.; Geng, S.; Liu, W.; Han, C. Investigation of the humping formation in the high power and high speed laser welding. *Opt. Lasers Eng.* **2018**, *107*, 102–111. [CrossRef]

15. Gullipalli, C.; Thawari, N.; Gupta, T.V.K. Humping defects in laser based direct metal deposition. *Mater. Today Proc.* **2023**. [CrossRef]
16. Shi, J.; Li, F.; Chen, S.; Zhao, Y.; Tian, H. Effect of in-process active cooling on forming quality and efficiency of tandem GMAW–based additive manufacturing. *Int. J. Adv. Manuf. Technol.* **2019**, *101*, 1349–1356. [CrossRef]
17. Montevecchi, F.; Venturini, G.; Grossi, N.; Scippa, A.; Campatelli, G. Heat accumulation prevention in Wire-Arc-Additive-Manufacturing using air jet impingement. *Manuf. Lett.* **2018**, *17*, 14–18. [CrossRef]
18. Montevecchi, F.; Venturini, G.; Grossi, N.; Scippa, A.; Campatelli, G. Idle time selection for wire-arc additive manufacturing: A finite element-based technique. *Addit. Manuf.* **2018**, *21*, 479–486. [CrossRef]
19. Singh, S.; Jinoop, A.N.; Kumar, G.T.A.T.; Palani, I.A.; Paul, C.P.; Prashanth, K.G. Effect of interlayer delay on the microstructure and mechanical properties of wire arc additive manufactured wall structures. *Materials* **2021**, *14*, 4187. [CrossRef]
20. Turgut, B.; Gürol, U.; Onler, R. Effect of interlayer dwell time on output quality in wire arc additive manufacturing of low carbon low alloy steel components. *Int. J. Adv. Manuf. Technol.* **2023**, *126*, 5277–5288. [CrossRef]
21. Dababneh, F.; Taheri, H. Investigation of the influence of process interruption on mechanical properties of metal additive manufacturing parts. *CIRP J. Manuf. Sci. Technol.* **2022**, *38*, 706–716. [CrossRef]
22. Denlinger, E.R.; Heigel, J.C.; Michaleris, P.; Palmer, T.A. Effect of inter-layer dwell time on distortion and residual stress in additive manufacturing of titanium and nickel alloys. *J. Mater. Process. Technol.* **2015**, *215*, 123–131. [CrossRef]
23. Alfaro, S.C.A.; Vargas, J.A.R.; De Carvalho, G.C.; De Souza, G.G. Characterization of "humping" in the GTA welding process using infrared images. *J. Mater. Process. Technol.* **2015**, *223*, 216–224. [CrossRef]
24. Xue, B.; Chang, B.; Du, D. A vision based method for humping detection in high-speed laser welding. *J. Phys. Conf. Ser.* **2021**, *1983*, 012074. [CrossRef]
25. Lu, J.; Zhao, Z.; Han, J.; Bai, L. Hump weld bead monitoring based on transient temperature field of molten pool. *Optik* **2020**, *208*, 164031. [CrossRef]
26. Altenburg, S.J.; Straße, A.; Gumenyuk, A.; Maierhofer, C. In-situ monitoring of a laser metal deposition (LMD) process: Comparison of MWIR, SWIR and high-speed NIR thermography. *Quant. Infrared Thermogr. J.* **2022**, *19*, 97–114. [CrossRef]
27. Felice, R.A.; Nash, D.A. Pyrometry of materials with changing, spectrally-dependent emissivity-Solid and liquid metals. In Proceedings of the AIP Conference Proceedings, Los Angeles, CA, USA, 19–23 March 2012; Volume 1552, pp. 734–739. [CrossRef]
28. Emissivity Values for Metals, (n.d.). Available online: https://www.flukeprocessinstruments.com/en-us/service-and-support/knowledge-center/infrared-technology/emissivity-metals (accessed on 4 October 2023).
29. Slater, C.; Hechu, K.; Davis, C.; Sridhar, S. Characterisation of the solidification of a molten steel surface using infrared thermography. *Metals* **2019**, *9*, 126. [CrossRef]
30. Kirillov, A.; Mintun, E.; Ravi, N.; Mao, H.; Rolland, C.; Gustafson, L.; Berg, A.; Lo, W.-Y.; Dollar, P.; Girshick, R. Segment Anything. 2023. Available online: https://ai.facebook.com/research/publications/segment-anything/ (accessed on 4 October 2023).
31. Zhang, J.; Lyu, T.; Hua, Y.; Shen, Z.; Sun, Q.; Rong, Y.; Zou, Y. Image Segmentation for Defect Analysis in Laser Powder Bed Fusion: Deep Data Mining of X-Ray Photography from Recent Literature. *Integr. Mater. Manuf. Innov.* **2022**, *11*, 418–432. [CrossRef]
32. Blumenstiel, B.; Jakubik, J.; Kühne, H.; Vössing, M. What a MESS: Multi-Domain Evaluation of Zero-Shot Semantic Segmentation. 2023. Available online: https://arxiv.org/abs/2306.15521v3 (accessed on 14 April 2024).
33. Hassan, M.A.; ElMallah, R.; Lee, C.G. Approximate and Memorize (A&M): Settling opposing views in replay-based continuous unsupervised domain adaptation. *Knowl.-Based Syst.* **2024**, *293*, 111653. [CrossRef]
34. Abubakr, M.; Akoush, B.; Khalil, A.; Hassan, M.A. Unleashing deep neural network full potential for solar radiation forecasting in a new geographic location with historical data scarcity: A transfer learning approach. *Eur. Phys. J. Plus* **2022**, *137*, 474. [CrossRef]
35. Segment Anything | Meta AI, (n.d.). Available online: https://segment-anything.com/ (accessed on 14 April 2024).